

**Chapter: Linkages between the radiation
belts, polar atmosphere and climate:
electron precipitation through wave
particle interactions**

M. A. Clilverd

British Antarctic Survey (NERC), Cambridge, UK

C. J. Rodger

Department of Physics, University of Otago, Dunedin, New Zealand

M. E. Andersson, A. Seppälä, and P. T. Verronen

Finnish Meteorological Institute, Helsinki, Finland

OXFORD
UNIVERSITY PRESS

Acknowledgements

M. A. Clilverd was supported by the NERC project NE/J008125/1. C. J. Rodger was supported by the New Zealand Marsden Fund. M. E. Andersson and P. T. Veronen were supported by the Academy of Finland (Projects #136225 and #140888). A. Seppälä was supported by the Academy of Finland (Projects #258165 and #265005).

Contents

1	Linkages between the radiation belts, polar atmosphere and climate: electron precipitation through wave particle interactions	1
1.1	Introduction	1
1.2	Overview of Coupling Process	2
1.3	Waves Driving Precipitation	4
1.4	Variations in Precipitation	6
1.5	Atmospheric Impact of Electron Precipitation	7
1.6	Linkages to Polar Surface Climate	14
	References	19

1

Linkages between the radiation belts, polar atmosphere and climate: electron precipitation through wave particle interactions

1.1 Introduction

The space around the Earth is filled with fast moving particles trapped in our magnetic field. These particles are principally electrons and protons, forming two "belts" separated by a "slot" region. The belts were initially discovered (Van Allen and Frank, 1959) in 1958 by the first US satellite, Explorer I, and were named the "Van Allen radiation belts" in honour of their discoverer, James Van Allen of the University of Iowa. As most satellites spend their lives inside the radiation belts, they are directly affected by this environment. Earth-orbiting satellites can be damaged or even lost (Lam *et al.*, 2012; Clilverd *et al.*, 2012) due to increased high-energy electron fluxes in the Earth's radiation belts (Van Allen and Frank, 1959; Millan and Baker, 2012). In particular, the outer radiation belt (located 3.5–8 Earth radii from the Earth's centre) is highly dynamic (Thorne, 2010; Horne *et al.*, 2005), with fluxes changing by 1000 times on timescales of hours to days (Morley *et al.*, 2010a; Baker *et al.*, 2004).

This high dynamism is due to large and rapid changes in the fluxes in the particles, caused by the acceleration and loss of energetic radiation belt electrons during and after geomagnetic storms (e.g., Reeves *et al.*, 2003). One of the major routes for the loss of these electrons is into the atmosphere (Green *et al.*, 2004; Millan and Thorne, 2007), in a process termed "precipitation". Due to the configuration of the geomagnetic field, the outer radiation belt electrons precipitate into the polar atmosphere, depositing energy into the mesosphere and upper stratosphere. This precipitation alters the ionisation rate over a wide altitude range; a 20 keV electron deposits the majority of its energy at an altitude slightly below 100 km, but higher energy electrons penetrate into the atmosphere more deeply, such that a ~ 4 MeV electron causes the largest changes at 40 km altitude (Turunen *et al.*, 2009), directly altering the ionospheric electron number density (and hence conductivity).

In Fig. 1.1 we show the altitudes versus ionisation rate for mono-energetic electron beams with a flux of $100 \text{ electrons cm}^{-2}\text{s}^{-1}\text{sr}^{-1}$. The energy ranges span from 20 keV to 4 MeV, representing relatively high energy auroral electrons through to relativistic electron precipitation. The electron ionisation rates make use of the expressions given

2 Electron precipitation through wave particle interactions

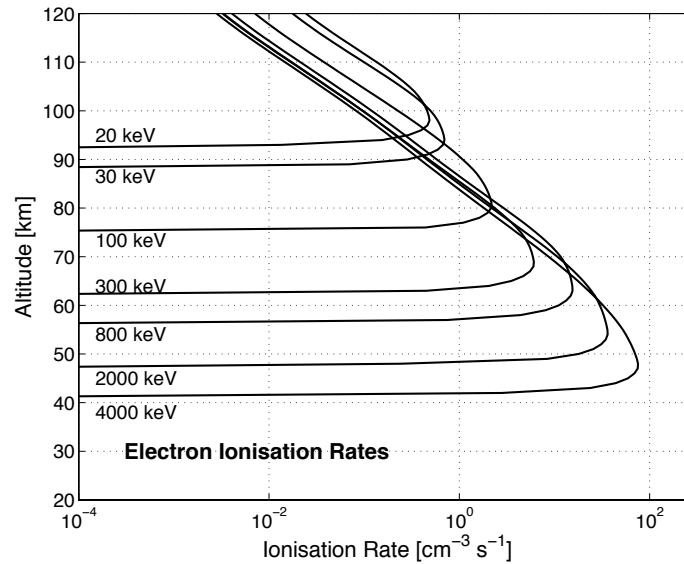


Fig. 1.1 Altitude versus ionisation rate for mono-energetic electron beams with a flux of 100 electrons $\text{cm}^{-2}\text{s}^{-1}\text{sr}^{-1}$.

by Rees (1989), and the individual lines represent energies of interest in terms of satellite measurements often discussed in this publication, i.e., POES and GOES electron detectors.

In this chapter we report on the processes by which plasma waves occurring in the space around the Earth can drive precipitation, generating excess ionisation at altitudes of 40–100 km, affecting the polar atmosphere and coupling to surface climate. The study of these processes includes observations from the ground, balloons and satellites, as well as modelling and climate data itself. This is an example of the multi-disciplinary nature of modern geophysics.

1.2 Overview of Coupling Process

When considering the linkages between the radiation belts, polar atmosphere and climate, via electron precipitation driven by wave particle interactions, we are envisaging the flowchart shown in Fig. 1.2. The fundamental driver of the system can be thought of as the geomagnetic storm, where processes energize the radiation belt particles, either through, or as a consequence of, wave-particle interactions. What drives the geomagnetic storm has been a topic of many of the previous chapters in this book and space physics texts (e.g., Hargreaves, 1992), and thus we do not consider it further here.

As a result of the geomagnetic storm, both VLF and ULF waves are enhanced, which in turn, can enhance the transport of electrons within the outer radiation belt and also drive wave-particle interactions between energetic electrons and magnetospheric waves such as VLF chorus, plasmaspheric hiss, electromagnetic ion cyclotron

waves (EMIC), and Pc5 micropulsations. These interactions are known to accelerate electrons from seed populations of ~ 30 keV to energies of >1 MeV while at the same time perturbing a fraction of the trapped population onto paths which are likely to interact with the Earth's atmosphere (e.g. Thorne, 2010, and references within; Omura and Zhao, 2013). Electrons which magnetically mirror at altitudes that are so low that they will hit the neutral atmosphere and be lost are said to be in the bounce-loss cone (BLC). This threshold altitude is generally set at ~ 100 km, although the literature include studies with thresholds ranging from 90–120 km. Mirroring altitudes vary with the strength of the Earth's magnetic field and thus with latitude and longitude. In and around the longitudes of the South Atlantic Magnetic Anomaly (SAMA) the mirror altitudes are at their lowest for a fixed geomagnetic latitude, and thus electrons that successfully mirror at other longitudes might still scatter in this region as they drift around the Earth. These electrons are said to be in the drift-loss cone (DLC) mirroring hundreds of kilometres above the atmosphere for most longitudes, but will be lost into the atmosphere in the SAMA-region. More detailed descriptions on the basic properties of the radiation belts may be found elsewhere (e.g. Walt, 1984; Spjeldvik and Rothwell, 1985). From a radiation belt physics perspective both BLC and DLC electrons are lost from the belts via precipitation, however, to the atmosphere the distinction is significant and can result in regions of preferential electron precipitation into the atmosphere.

Due to the Earth's magnetic field configuration, energetic particle precipitation occurs mainly in the polar auroral and sub-auroral regions, *i.e.*, at latitudes higher than 45° . The altitudes at which these particles deposit their momentum is dependent on their energy spectrum, with lower energy particles impacting the atmosphere at higher altitudes than their more energetic relatives (Rees, 1989; Rodger *et al.*, 2007). Precipitating charged particles produce NO_x ($\text{NO}_x = \text{N} + \text{NO} + \text{NO}_2$) and HO_x ($\text{HO}_x = \text{H} + \text{OH} + \text{HO}_2$) through ionisation or dissociative ionisation of N_2 and O_2 molecules, which results in the formation of N_2^+ , O_2^+ , N^+ , O^+ , and NO^+ , and subsequent ion chemistry (Verronen and Lehmann, 2013). This is shown schematically in Fig. 1.2.

Modelling and experimental observations have demonstrated significant chemical alterations, particularly in the concentrations of odd nitrogen (NO_x) and odd hydrogen (HO_x), which can catalytically destroy ozone (Crutzen, 1970; Brasseur and Solomon, 2005). For some time it has been recognized that very intense energetic particle precipitation (EPP) events could lead to significant ozone destruction in the polar middle atmosphere, which was subsequently experimentally observed during solar proton events (e.g., Seppälä *et al.*, 2004; Seppälä *et al.*, 2006). However, there has also been growing evidence that geomagnetic storms produce high fluxes of energetic electron precipitation (e.g. Rodger *et al.*, 2007), with modelling suggesting energetic electron precipitation can also lead to significant mesospheric chemical changes in the polar regions (Rodger *et al.*, 2010) affecting the chemical makeup of the polar atmosphere.

The radiative balance of the atmosphere is driven by its composition, particularly through the abundance of ozone and its capability of absorbing solar UV radiation efficiently (Brasseur and Solomon, 2005). As NO_x and HO_x influence the ozone abundance at upper stratosphere and mesospheric levels, the radiative balance can be

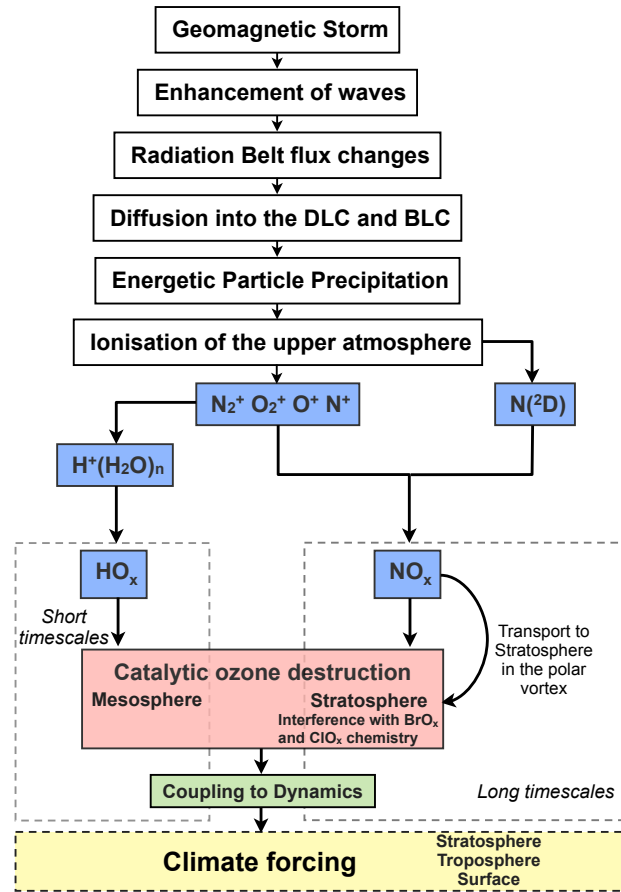


Fig. 1.2 Flowchart depicting the linkage from radiation belt to climate.

altered. Through this mechanism atmospheric wind patterns can be affected, influencing the propagation of atmospheric waves within the stratosphere and troposphere. As Fig. 1.2 shows, this step-by-step process provides a pathway to link geomagnetic storm perturbations in the radiation belts, with chemical changes in the upper atmosphere, and ultimately, with the dynamics of the lower atmosphere. In the next sections we will describe each of these links in more detail.

1.3 Waves Driving Precipitation

Previous chapters in this book have highlighted the types of waves that can energy exchange with outer radiation belt electrons through gyroresonant interactions. Magnetospheric wave modes include whistler-mode chorus outside of the plasmasphere, electromagnetic ion cyclotron waves (EMIC) on or around the plasmopause, and whistler-

mode hiss inside the plasmasphere. Whistler mode chorus can accelerate electrons to higher energies, while chorus, hiss and EMIC waves can all scatter electrons into the DLC and BLC through resonant pitch angle scattering. Other losses of radiation belt electrons can occur through radial diffusion and magnetopause shadowing. However, in this chapter we are particularly interested in the loss into the atmosphere of electrons as a result of pitch angle scattering. As an electron drifts in longitude it may well experience each of these wave modes within one orbit of the Earth, depending on the L-shell of the drift orbit. As a result, all of the wave modes may contribute to the overall rates of electron precipitation, with different contributions occurring for different electron energies (Horne, 2002). The schematic of the distributions of chorus, plasmaspheric hiss, and EMIC waves relative to the shape of the plasmasphere shown in Summers *et al.* (2007) encapsulates the picture we have in mind here.

Although the DLC is only a small fraction of the pitch angle distribution of electrons when compared with the BLC it does play an important role as far as the atmospheric impact of radiation belt electrons is concerned. When electrons are scattered towards the loss-cone from quasi-trapped pitch angles they will either diffuse deep into the BLC or remain close to the outer edge of the BLC, i.e., the DLC. In these cases the diffusion is known either as strong or weak (Kennel and Petschek, 1966). Calculations of bounce-averaged quasi-linear diffusion coefficients for chorus, hiss, and EMIC waves have shown that the scattering strength is dependent on the wave mode type, the electron energy, the amplitude and the distribution of the waves, and the plasma density distribution (Summers and Thorne, 2003; Summers *et al.*, 2007). If strong diffusion dominates the pitch angle scattering process, driving electrons into the BLC, any precipitation will be independent of geographic longitude. However, if weak diffusion dominates, the DLC comes more into play, and a bias would be expected with geographic longitude, particularly in the southern hemisphere around the SAMA.

Key to the type and efficiency of pitch angle diffusion of any given wave mode are the amplitude and latitudinal distribution of the waves. Meredith *et al.* (2003) have shown the MLT and L-shell distributions of chorus for non-disturbed, moderately-disturbed, and severely-disturbed geomagnetic activity levels. Typically the regions of intense chorus waves increase in MLT and L-shell range as geomagnetic activity is enhanced. Chorus occurs in two frequency bands, spanning either side of the half electron gyrofrequency ($f_{ce}/2$). In Fig. 1.3 we show the lower band chorus intensity ($0.1 - 0.5 f_{ce}$) as a function of latitude and longitude as observed by the low altitude satellite DEMETER for quiet ($Kp < 4$) and disturbed ($Kp \geq 4$) geomagnetic conditions. The intensity of the observed chorus waves is 2-3 orders of magnitude higher during periods of disturbed geomagnetic activity than during non-disturbed conditions. No significant variations in longitude are observed, and no hemispheric bias is present either. However, over the typical range of DEMETER observations ($2 < L < 5$) there is a noticeable increase in wave intensity with increasing geomagnetic latitude. Increasing wave intensity with geomagnetic activity is likely to change the pitch angle scattering regime from one of weak diffusion to strong diffusion, depending on the electron energy, and thus change the precipitation patterns from a South Atlantic DLC-dominated picture into a more uniformly distributed BLC-dominated picture.

6 Electron precipitation through wave particle interactions

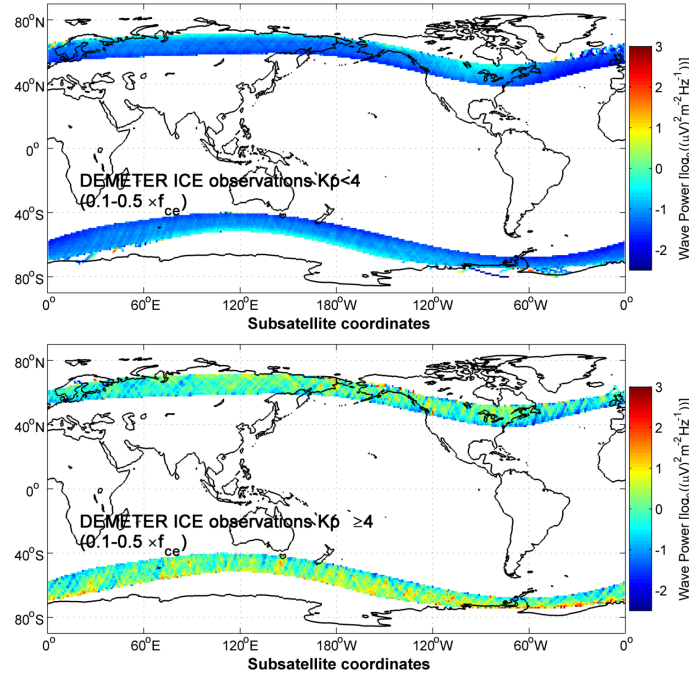


Fig. 1.3 DEMETER lower band chorus wave maps, showing variation with Kp, representing quiet and disturbed geomagnetic activity conditions.

1.4 Variations in Precipitation

One way to study the linkage between geomagnetic activity, the dynamic nature of the outer radiation belt trapped electron fluxes, and electron precipitation into the atmosphere, is through the analysis of geomagnetic storms triggered by the arrival of a high speed solar wind stream interface (SWSI) and associated dropouts in energetic electron fluxes (e.g., Morley *et al.*, 2010*b*). In the Morley statistical studies, utilizing 9 GPS-borne particle detectors, a superposed epoch analysis around the arrival of 67 SWSIs showed a strong repeatable "signal" of a rapid electron flux dropout (Morley *et al.*, 2010*a*) followed by a recovery with higher trapped electron fluxes. Hendry *et al.* (2012) used the Morley epochs to show that the dropouts in trapped flux are followed ~ 3 hours later by large increases of electron precipitation into the atmosphere. These precipitation events appear to be associated with the time that the trapped electron fluxes begin to recover rather than the dropouts themselves, and may signify that a simultaneous acceleration and loss process is in operation. We make use of the Morley epochs again in showing the link between geomagnetic storms, wave intensities, and electron precipitation. Figure 1.4 shows the superposed analysis of the geomagnetic index Kp, the DEMETER lower band chorus wave intensity, and the POES satellite observed >100 keV electron precipitation flux for the Morley epochs. The POES >100 keV electron precipitation fluxes show similar temporal and L-shell variations as

the DEMETER wave panel. As expected the Kp index increases at epoch day 0 with a steady recovery back to pre-storm levels by about day 5. The DEMETER chorus wave intensities show an increase of about 2 orders of magnitude at epoch day 0, with a recovery lasting about 5 days. High electron precipitation fluxes are triggered by the geomagnetic storm and extend from L=7 (the observational limit of DEMETER) to L=4.5 at the peak of the geomagnetic disturbance, with magnitude increases of a factor of ~ 1.5 . In this case the POES fluxes are zonally averaged, and provide no information about the relative contributions of BLC and DLC flux.

The L-shell over which the chorus waves are observed increases as a result of the geomagnetic storm, with an expansion to lower L-shells that mirrors the dynamic behaviour of the plasmapause. The lower L-shell boundary of the electron precipitation also mirrors the expected behaviour of the plasmapause and is consistent with the storm event analysed in detail by Lichtenberger *et al.* (2013). From Fig. 1.4 we can infer that there is a strong correspondence between chorus wave intensity and electron precipitation flux, and that it is primarily associated with regions outside of the plasmasphere. Given the work of Hendry *et al.* (2012) it is possible that the waves are contributing to the acceleration of energetic electrons in the outer radiation belt, while at the same time enhancing the loss of a fraction of those electrons to the atmosphere, i.e., in the pumping up and subsequent draining of the radiation belts.

1.5 Atmospheric Impact of Electron Precipitation

Energetic electron precipitation into the atmosphere results in the ionisation of neutral constituents, particularly in the polar regions as a result of the configuration of the Earth's magnetic field. Strong ionisation sources can enhance the ion pair production levels in the D-region above that provided by Lyman-alpha radiation and EUV (Brasseur and Solomon, 2005). Electron precipitation contributes to the production of odd nitrogen NO_x ($\text{N} + \text{NO} + \text{NO}_2$) through the dissociation of molecular nitrogen, and odd hydrogen HO_x ($\text{H} + \text{OH} + \text{HO}_2$) through chemistry associated with ion pair production, water cluster ion formation, and subsequent neutralization (Verronen and Lehmann, 2013). A schematic of this process is shown in Fig. 1.2.

NO_x can have a long chemical lifetime (months) if it is produced in the dark polar wintertime when it can be transported to lower altitudes and latitudes, or if it's produced directly at stratospheric altitudes (Siskind *et al.*, 1997). HO_x has a short chemical lifetime (hours) and so is generated by electron precipitation in-situ, and only for as long as the ionisation continues. Both NO_x and HO_x can destroy odd oxygen through catalytic reactions, and hence play an important role in the ozone balance of the middle atmosphere. As NO_x and HO_x have such different characteristics, we consider them separately in the following sections.

1.5.1 Odd Nitrogen

When we consider NO_x that is created by energetic electron precipitation, we are primarily interested in that produced in the polar regions during the dark wintertime. In these conditions the NO_x gases can survive for long periods, and be transported significant distances, particularly horizontally by winds within the stratospheric polar vortex, and vertically by subsiding air masses at the winter pole. As a result of

8 Electron precipitation through wave particle interactions

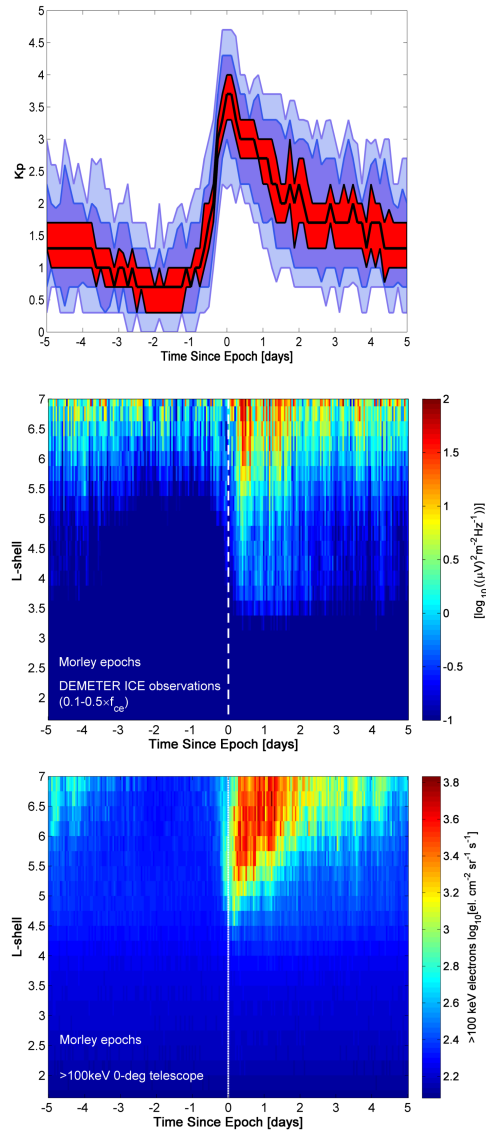


Fig. 1.4 DEMETER chorus wave and POES electron precipitation characteristics during the Morley superposed epoch geomagnetic storm events. The superposed epoch median of the quantity is given by a black line. The 95% confidence interval for the median is given by the red band. The blue bands mark the interquartile range and the 95% confidence interval about it (light blue).

these transport conditions, it is difficult to separate the contribution of in-situ direct formation of NO_x by electron precipitation, and indirect NO_x being transported from another region where it could have been generated at a different altitude by electron precipitation with different energy.

A simple picture would be of a wintertime column of enhanced NO_x generated by particle precipitation from 40–120 km, and confined to a region polewards of 60° (geographic latitude) by the stratospheric polar vortex. At the summer pole the abundance of NO_x would be lower due to photodissociation from solar radiation, and the absence of the polar vortex. This picture is complicated by the time varying nature of electron precipitation due to geomagnetic storms, the radiation belt processes that influence the type of wave modes that act to scatter electrons, and the dynamic behaviour of the stratospheric polar vortex (Solomon *et al.*, 1999; Harvey *et al.*, 2009).

Direct NO_x production by radiation belt electron precipitation has been observed by the sub-mm radiometer at Troll, Antarctica, during the winter of 2008 (Newnham *et al.*, 2011). NO was observed at 70–80 km altitudes at L=4.5 following a geomagnetic storm, and was well correlated with ~ 300 keV electron precipitation energies observed by POES. In a superposed epoch analysis of recurrent geomagnetic storms at the same site Newnham *et al.* (2013) confirmed the direct production of 70–80 km NO by radiation belt electron precipitation, but also observed a second NO signature at 70–80 km ~ 7 days after the geomagnetic storm. The second pulse of NO could be a result of downward transport of auroral NO_x created by lower energy electron precipitation, or horizontal transport. Given the long lifetime of NO_x in wintertime conditions it is difficult to be certain of the ionisation source without high quality modelling of atmospheric transport conditions.

Indirect NO_x has been observed by satellites, and its transport to lower altitudes studied extensively. Randall *et al.* (2005, 2007, 2009) analysed several indirect NO_x events that occurred during the northern hemisphere wintertime. Enhancements of NO_x were observed to descend from ~ 80 km altitude to ~ 30 km altitude over several months, with descent rates of 5–10 km/month. Although an overall descent of winter polar air is expected, the enhanced NO_x was particularly associated with sudden stratospheric warmings (SSW), where the stratospheric polar vortex is disrupted and then formed again, with the stratopause occurring at much higher altitudes than normal. Thus the enhanced NO_x is likely to have originated at altitudes as high as the aurora at >100 km. The electron precipitation that generates the NO_x under these circumstances is likely to be relatively soft, with energies of <30 keV, or possibly auroral energies of only 1 keV or so. However, when high energy electron precipitation events occur during an indirect NO_x descent period it will add to the abundance of NO_x at the appropriate altitude for the energy, and be transported down to the stratosphere as well (Clilverd *et al.*, 2009).

There are significant differences in the occurrence of indirect NO_x events in the northern and southern hemisphere. In the southern hemisphere the stratospheric polar vortex forms regularly each winter and transports NO_x down into the stratosphere in most years (Randall *et al.*, 2007). In the northern hemisphere the wintertime polar vortex is affected by the highly varying dynamical conditions and is often disrupted during the course of the winter. As a result indirect NO_x enhancements are only

10 Electron precipitation through wave particle interactions

intermittently observed during the winter in the northern hemisphere (Seppälä *et al.*, 2007; Randall *et al.*, 2009).

In the stratosphere NO_x catalytically destroys ozone. The combination of direct and indirect NO_x sources makes attribution of stratospheric ozone changes more challenging, particularly when considering the influence of radiation-belt processes in preference to auroral production. However, Clilverd *et al.* (2009) reported the observation of enhanced direct NO_x at ~ 50 km generated by relativistic electron precipitation (~ 2 MeV), and the subsequent reduction of ozone at altitudes as low as 40 km. Randall *et al.* (2005) showed that large enhancements of NO_x transported downwards in the northern hemisphere polar vortex caused long lasting ozone reductions at 40 km altitude from March to at least July 2004. The NO_x was generated at mesospheric and upper stratospheric altitudes as a result of large geomagnetic storms in October and November 2003, with contributing geomagnetic activity continuing into January 2004. Vertical transport times for the NO_x to travel from ~ 80 km to 40 km altitudes were about 3 months, and the NO_x influence on ozone lasted for a further 4 months, indicating that NO_x effects can be long-lasting and significantly displaced from the generation region.

Rodger *et al.* (2010) showed that direct radiation-belt electron precipitation occurring at $L=3$ during a large geomagnetic storm could increase NO_x abundance by 80% at 60-75 km altitudes, and decrease ozone by up to 35%, with the effect lasting beyond a week. The calculations were undertaken by the Sodankylä Ion and Neutral Chemistry model (SIC), which includes a comprehensive description of the ion chemistry involved (Verronen *et al.*, 2005). The results showed that the large initial short-term ozone depletion peaks were caused by HO_x , with a smaller, but longer lasting ozone loss arising from the NO_x enhancements. Figure 1.5 shows the change in ionisation from 50-100 km due to the 70 keV-2.5 MeV electron precipitation fluxes that were calculated during a large geomagnetic storm (-130 nT) that occurred in September 2005, the resulting NO_x enhancements, and consequent ozone reductions that would be produced at $L=3$ in the southern hemisphere if polar winter conditions (i.e., if the storm occurred in July) were applied. The level of ozone reduction in this case is equivalent to that of a large solar proton event, lasts longer than a typical solar proton event, and has the potential to occur more frequently throughout the 11-year solar activity cycle (Rodger *et al.*, 2010).

More recently Daae *et al.* (2012) reported the ground-based observation of an enhancement of direct NO_x generated in-situ by electron precipitation (~ 300 keV) during a geomagnetic storm in 2009, with a co-incident 17–67% reduction of ozone abundance between 70–75 km. It is likely that much of the initial ozone depletion was caused by HO_x generated at the same time as the NO_x (Verronen *et al.*, 2013), although only NO_x is able to survive long enough to descend towards the stratosphere influencing ozone abundance along the way, as was observed. Attribution of the influence of energetic electron precipitation on ozone is one of a combined role of NO_x and HO_x production during the precipitation event, with NO_x having a longer-term influence after the precipitation ceases, involving horizontal and vertical transport. The production of HO_x by energetic electron precipitation is discussed in more detail in the next section.

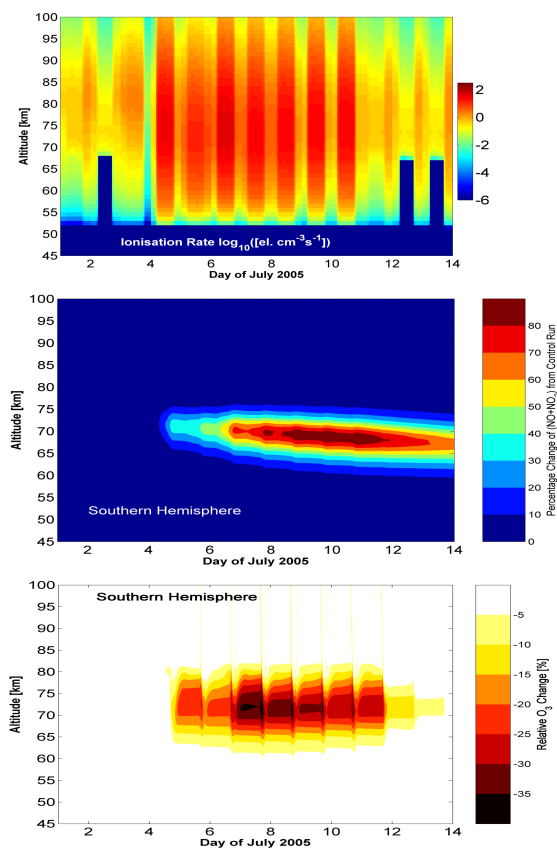


Fig. 1.5 Modelling the impact of radiation-belt electron precipitation between 45–100 km during an electron precipitation event at $L=3$ in wintertime in the southern hemisphere. Top panel: ionisation levels, middle panel: NO_x abundance, and bottom panel: O_3 destruction.

1.5.2 Odd Hydrogen

In polar regions energetic electron precipitation can enhance HO_x as a result of production through ionisation and water cluster ion chemistry (Verronen and Lehmann, 2013). Below altitudes of 80 km there is enough H_2O for water cluster ion formation, and at these altitudes the chemical lifetime of HO_x is up to a day. Thus HO_x concentrations respond rapidly to electron precipitation events, and are not subject to the influence of significant horizontal or vertical transport once the precipitation forcing finishes. Taking advantage of this property means that HO_x can be used to monitor the regions and altitudes over which electron precipitation from the outer radiation belt occurs.

The first observation of OH production due to energetic electron precipitation was published by Verronen *et al.* (2011). They found a strong correlation between 100–300 keV loss cone electron count rates observed in the outer radiation belt by POES

12 Electron precipitation through wave particle interactions

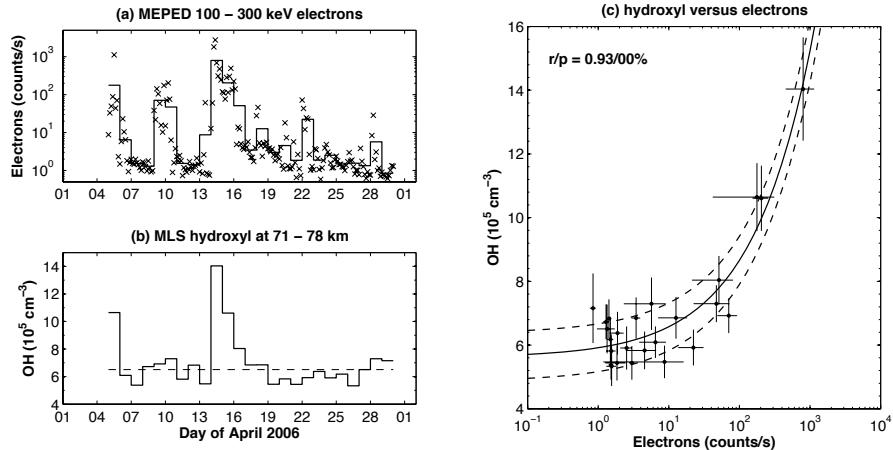


Fig. 1.6 OH concentration at 71–78 km versus electron count rate during April 2006. (a) 3-hour (X) and daily (solid line) mean electron count rates measured by MEPED. (b) Daily mean OH concentrations measured by MLS. (c) Daily mean OH versus daily mean electrons (dots). Horizontal and vertical lines mark the standard error of the mean. The solid and dashed lines mark a line fit and its estimated standard deviation. r is the correlation coefficient and p is the related random chance probability.

MEPED, and the night-time OH concentrations in the middle mesosphere at 71–78 km altitude observed by the Microwave Limb Sounder (MLS) on board the Aura satellite. At 55–65° magnetic latitude ($L=3.0$ –5.6) increases in electron precipitation by two orders of magnitude were accompanied by increases in night-time OH concentration of 100%. In Fig. 1.6 we summarise the findings made by Verronen *et al.* (2011) showing the POES MEPED and MLS data from April 2006. A large geomagnetic storm occurred on 13 April which was followed by high fluxes of 100–300 keV electron precipitation into the atmosphere. High concentrations of OH were observed at 70–78 km altitudes, which as Fig. 1.6 shows, is consistent with in-situ ionisation from 100–300 keV electron precipitation. The relationship between the two parameters is given in the panel on the right, with a linear fit (solid line) and standard deviations (dashed lines) shown. In this monthly case, over 85% (r^2) of the OH daily variation could be explained by changes in radiation belt electron precipitation.

Andersson *et al.* (2012) extended the study period to 2004–2009, also comparing POES and MLS nighttime data on a month by month basis. Over the 55–65° magnetic latitude range ($L=3.0$ –5.6) high correlation between POES electrons and MLS OH was found when high fluxes of 100–300 keV precipitating electrons were observed, while 34% of the 65 months analysed showed clear correlation. The highest correlations were found at 75 km altitudes, although the influence on OH production by electron precipitation was detected as low as 52 km, equivalent to fluxes of ~ 3 MeV electrons. Similar results were found in both hemispheres, and clear effects on OH production were found over the 55–72° magnetic latitude range ($L=3.0$ –10). Thus, radiation belt forcing of chemical change in the upper atmosphere (50–80 km) was confirmed and shown to be

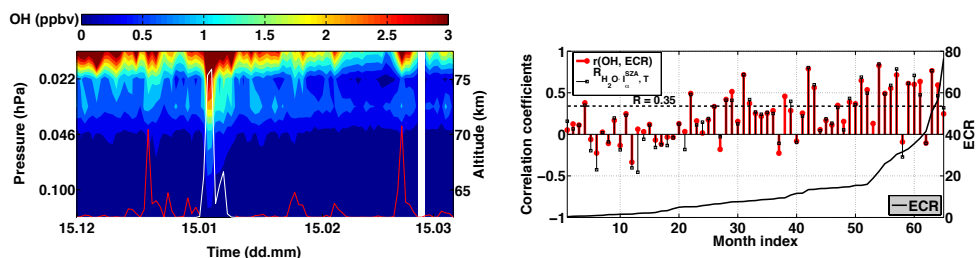


Fig. 1.7 Left panel: Daily mean OH mixing ratio (ppbv) at geomagnetic latitudes $55\text{--}65^\circ$ shown for altitudes 63–78 km for the period 15th of December 2004 to 15th of March 2005. Daily mean electron count rate (ECR) is marked with a red line and daily mean proton fluxes are marked as white line. Right panel: Correlation r (red bar) and partial correlation (black line) between OH and ECR at $55\text{--}65^\circ$ shown for altitude 75 km (0.022 hPa) sorted in ascending order by monthly mean ECR.

a significant influence on the overall variability of HO_x at mid-high latitudes in both hemispheres. Figure 1.7 provides an example of the analysis undertaken by Andersson *et al.* (2012) showing 3 months of MLS OH observations (left panel) and the month by month correlation analysis, with the months sorted by electron count rate (ECR) on the 100–300 keV range.

The analysis of MLS OH observations has also been used to investigate the impact of weak and strong scattering processes that take place in the outer radiation belt. Andersson *et al.* (2013) showed that during periods of high POES 100–300 keV electron count rate more OH was produced in the southern hemisphere than the northern hemisphere, and that the majority in the south occurred in the region of the Weddell Sea poleward of the SAMA (-120° to 60°E). As discussed earlier in this chapter, the bias towards the Weddell Sea region is indicative of the dominance of weak diffusion processes preferentially pushing electrons into the DLC. Figure 1.8 shows the geographic variation of MLS nighttime OH concentration at 75 km, with the left panel representing disturbed geomagnetic conditions ($K_p > 4$) and the right panel representing quiet geomagnetic conditions ($K_p < 4$). $L=3$ and $L=10$ contours are plotted for both hemispheres as white lines, representing the footprint of the outer radiation belt super-imposed on the atmosphere. From Fig. 1.8 we can take two things: 1) during quiet geomagnetic conditions there is still some OH generation in the Weddell Sea region suggesting a background drizzle of electron precipitation from the outer radiation belt; 2) during high geomagnetic conditions the OH is observed over an almost continuous range of longitudes (particularly when both hemispheres are combined) and this suggests that strong diffusion into the BLC is taking place.

Once the HO_x has been generated by energetic electron precipitation it has the ability to catalytically destroy ozone. Verronen *et al.* (2013) used the daily mean electron energy flux spectrum, determined from POES and DEMETER electron precipitation detectors, to constrain the SIC model. The ionisation rate enhancements produced by the model were able to reproduce the day-to-day variability of OH and ozone observed

14 Electron precipitation through wave particle interactions

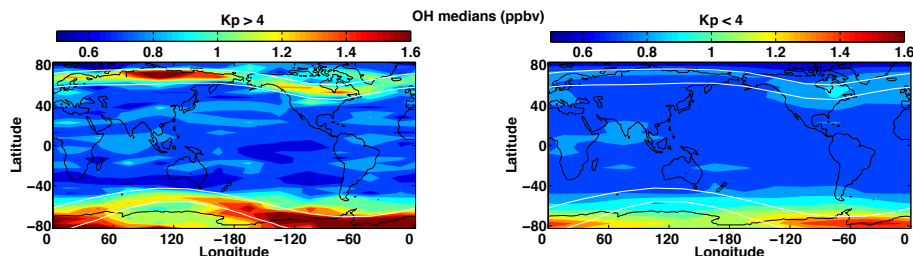


Fig. 1.8 Maps of OH volume mixing ratio for high ($K_p > 4$) and low ($K_p < 4$) geomagnetic activity levels. $L=3$ and $L=10$ contours are shown.

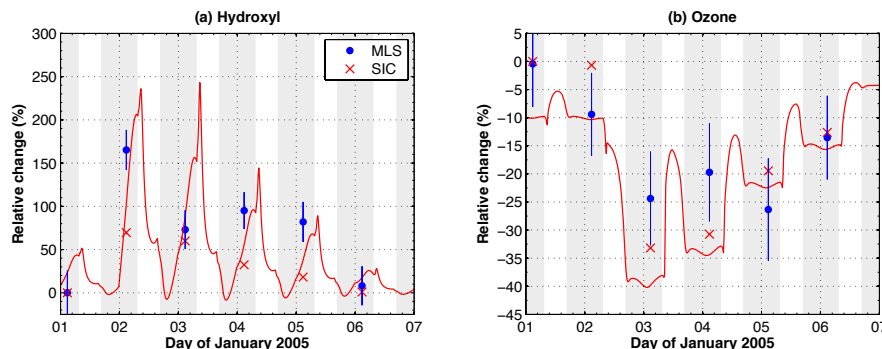


Fig. 1.9 Comparison between modelled and observed relative change of OH (a) and ozone (b) at 74 km for January NH. Red line: SIC data showing $100 \times (EPR/CTR - 1)$, where EPR and CTR are gas concentrations from the electron and control runs, respectively. Red X marks: Same as Red Line, except that CTR is replaced by 1st-day result from the electron precipitation run, and shown only at the local solar time of MLS observations. Blue circles: MLS data showing the change with respect to the observations on the day before the electron forcing peak. Grey shading marks the local times with solar zenith angle $> 100^\circ$, i.e. nighttime.

by MLS during four large precipitation events. Figure 1.9 shows the modelling results from SIC during an example geomagnetic storm in January 2005, at 74 km in the northern hemisphere. Overall, the model predicted OH increases at 60–80 km, reaching several hundred percent at 70–80 km during peak electron precipitation forcing. Increases in OH were followed by ozone depletion, of several tens of percent. The magnitude of modeled changes were not only similar to those observed by MLS, but were large enough to be comparable to the effects of individual solar proton events.

1.6 Linkages to Polar Surface Climate

Changes in the abundance of ozone in the stratosphere and mesosphere (30–100 km) can lead to changes in the radiative balance of the atmosphere. In this section we describe the analysis that has led to an increased understanding of the way in which

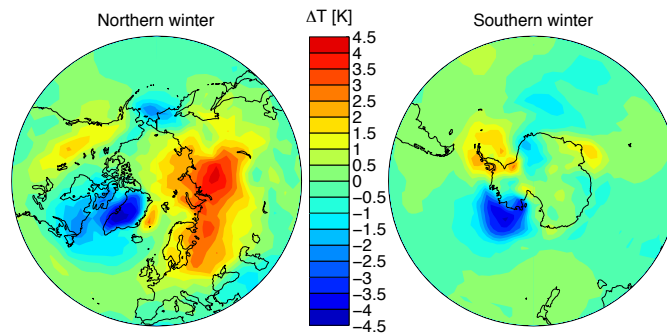


Fig. 1.10 Wintertime northern and southern hemisphere surface temperature differences for high geomagnetic activity (i.e., high A_p) – low A_p .

radiation belt processes not only link to the polar atmosphere, but could ultimately couple to polar climate.

1.6.1 Influence on Polar Climate

The influence of NO_x and HO_x chemistry on polar surface temperatures was first suggested by modelling results presented by Rozanov *et al.* (2005). The chemistry–climate model, UIUC CCM, was run with and without a NO_x source, generated by energetic particle precipitation between the upper stratosphere and lower-thermosphere. The resultant polar surface temperature changes were strongest during the winter months, and showed complex positive and negative temperature patterns which were different in each hemisphere. The conclusions of the study were that NO_x generated at high altitude by energetic electron precipitation was able to influence surface temperatures through the coupling of chemical and dynamical changes in the middle and upper atmosphere. This prediction was confirmed by Seppälä *et al.* (2009) who showed that the polar surface temperature differences found in ERA-40 re-analysis data, grouped into two subsets consisting of high and low geomagnetic activity, were consistent with Rozanov *et al.* (2005). The temperature ranges involved were ± 5 K, with some regions experiencing warmer winters when geomagnetic activity was high, and some experiencing cooler winters. Seppälä *et al.* (2009) also confirmed these regional findings with winter temperature analysis from individual meteorological sites. Figure 1.10 shows the wintertime northern and southern hemisphere surface temperature differences for high geomagnetic activity (i.e., high A_p) – low A_p . In the northern hemisphere the figure shows warming over Russia and Canada, and cooling over Greenland and the Bering Sea. In the southern hemisphere the figure shows warming over the Antarctic Peninsula, and cooling over the Bellingshausen Sea. Other regions show less structured variations.

These findings were confirmed by Baumgaertner *et al.* (2011) in a comprehensive analysis using the ECHAM5/MESSy Atmospheric Chemistry (EMAC) model. ECHAM5/MESSy includes submodels describing tropospheric and middle atmosphere processes and their interaction with oceans, land and human influences (Jöckel *et al.*,

2006). Baumgaertner *et al.* (2011) concluded that similar surface temperature patterns were found and were related to NO_x production due to increased geomagnetic activity and resultant energetic electron precipitation. The NO_x production leads to ozone depletion in the stratosphere which causes changes in the radiative budget and the mean meridional circulation. In the presence of sunlight ozone absorbs solar short-wave radiation resulting in heating of the atmosphere. An opposing effect is present in the absence of sunlight, such as during the dark polar winter, when ozone absorbs long-wave radiation from the surface, with the different wavelength range leading to a cooling effect (Langematz *et al.*, 2003). Ozone changes can therefore potentially lead to temperatures changes even during the polar night influencing the strength of the polar vortex (Langematz *et al.*, 2003). Associated positive stratospheric Northern Annular Mode (NAM) anomalies (and Southern Annular Mode SAM anomalies) propagate into the troposphere, where typical positive NAM/SAM surface pressure and temperature patterns occur, as were found by Seppälä *et al.* (2009). NAM and SAM are large scale patterns of climate variability arising from internal variation in atmospheric dynamics and they are recognised as the most important climate variability patterns at mid- and high latitudes, e.g. in horizontal and vertical wind and temperature fields. Enhanced geomagnetic activity and NO_x production appear to trigger positive NAM/SAM phases at the surface which are constrained to wintertime in the polar regions because of radiation belt source processes, and the complex interaction of chemistry and dynamical coupling in the atmosphere.

Further analysis of the stratosphere-troposphere coupling mechanism was undertaken by Seppälä *et al.* (2013). A re-analysis dataset from 1958–2012 was used to determine the high Ap and low Ap monthly zonal mean zonal wind anomalies (ΔU) and zonal mean temperature anomalies (ΔT) in the northern hemisphere. Figure 1.11 shows the extra-tropical (20–90° latitudes) wind and temperature monthly anomalies for December, January, and February for high Ap conditions. A region of strengthening zonal wind anomalies (more eastward) and warmer temperatures appear in the upper stratosphere and are observed to slowly descend in altitude at high latitudes. As a result, a stronger polar night jet persists longer than normal, with anomalously high polar winds across the stratosphere, i.e., a stronger polar vortex, resulting in positive NAM anomalies.

1.6.2 Possible Significance to Regional Weather Variability

Regional climate variability of the extra-tropical Northern Hemisphere (NH) is largely controlled by the NAM in the stratosphere, and its counter-part in the troposphere, the North Atlantic Oscillation (NAO). Under certain conditions, the low frequency effect of the NAM spans from the stratosphere into the troposphere (Baldwin *et al.*, 2003). Near the surface and over the North Atlantic region, the NAO and the NAM are almost indistinguishable from each other. The NAO is a large-scale mode (i.e., pattern) of climate variability that has major impact on the weather and climate either side of the North Atlantic, especially north-western Europe. Downward coupling of stratospheric circulation changes to the surface accounts for the majority of change in regional surface climate over Europe and North America (Scaife *et al.*, 2005). When the NAO/NAM is positive, there is a net displacement of Arctic air towards the subtropics

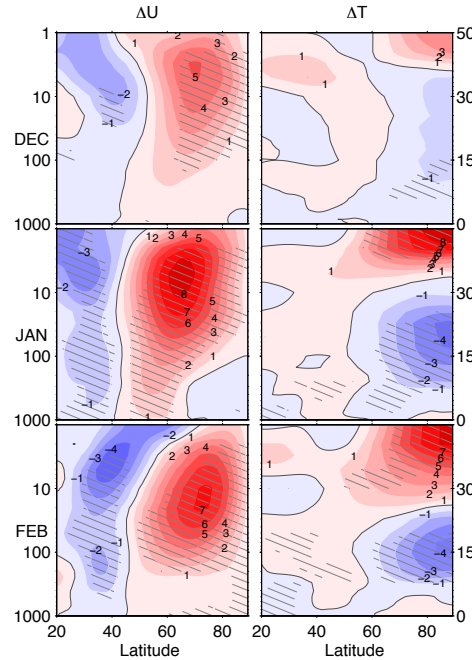


Fig. 1.11 Monthly zonal mean zonal wind anomalies (ΔU) and zonal mean temperature anomalies (ΔT) in the northern hemisphere for high A_p conditions. The atmospheric pressure levels in hPa are shown on the left and corresponding altitudes in km on the right. The shading corresponds to $\geq 90\%$ statistical significance levels.

near the Azores. This strengthens westerly winds in the North Atlantic resulting in warmer moist air flowing towards the adjacent regions, and milder maritime winters. In a negative NAM/NAO air displaces towards the Arctic, bringing weaker westerlies over the North Atlantic, and colder than normal maritime winters.

Stronger and more significant correlations have been found to exist between geomagnetic activity and the NAO than with the 11-yr solar UV cycle (Bochníček and Hejda, 2005), and solar wind dynamic pressure has been shown to be correlated with the winter NAM (Lu *et al.*, 2008). To study the relationship between geomagnetic forcing and the NAO during the northern hemisphere winter, Li *et al.* (2011) analysed the 150-year time series of the geomagnetic aa index. Over the whole 150 year period studied only about 8% of the variance in wintertime NAO is explained by the wintertime aa index. However, the aa-NAO relationship becomes clearer and more robust statistically when only the data from the declining phase of even-numbered 11-year solar cycles are included. This may be related to the dominant polarity of the interplanetary magnetic field with respect to the ecliptic plane, as energy shifts between the Sun's toroidal and poloidal magnetic fields. In this case 34% of the variance of the winter NAO can be explained by the geomagnetic aa index. Thus, in the northern

hemisphere, geomagnetic forcing of NAO weather patterns is strongly associated with the declining phase of the 11-year solar cycle. This phase of the cycle is characterised by recurrent geomagnetic activity which drives large changes in outer radiation belt acceleration and loss processes, involving storms which are of long duration, and produce high fluxes of relativistic electrons (Borovsky and Denton, 2006). All these observations are consistent with the idea that radiation belt electron precipitation fluxes play a role in atmospheric chemistry and dynamics, ultimately linking to surface climate variability.

In the southern hemisphere the equivalent to the NAM is the southern annular mode (SAM). The coupling of radiation belt electron precipitation into the upper atmosphere has many similarities with the northern hemisphere, although key processes show differences, such as the increased stability of the wintertime polar vortex over Antarctica. Seppälä *et al.* (2009) found clear indications of geomagnetic activity impact on polar surface temperatures, with patterns that are consistent with the modulation of the SAM. Other work has shown the influence of the SAM on rainfall precipitation over New Zealand, and thus indicates the potential of geomagnetic activity influence on southern hemisphere regional weather variability (Renwick and Thompson, 2006).

As outlined throughout this chapter, wave-particle interaction processes in the outer radiation belt scatter energetic electrons into the atmosphere creating excess ionisation. The processes influence the locations and altitudes of the chemical changes, through defining the electron energies involved, the location of the wave-particle interaction regions relative to the plasmopause, and the strength of the pitch-angle diffusion taking place. The ionisation produced in the upper atmosphere results in the generation of NO_x and HO_x species, which can catalytically destroy ozone. Resultant changes in atmospheric dynamics propagate down into the troposphere and modulate the wintertime weather patterns in the northern and southern hemispheres. In recent years the linkage between the radiation belts, energetic electron loss processes, the atmosphere, and regional climate variability has been investigated with increasing understanding. However, details about the exact coupling mechanism, and its impact on climate, still need to be fully determined.

References

- Andersson, M. E., Verronen, P. T., Rodger, C. J., Clilverd, M. A., and Wang, S. (2013). *Atmos. Chem. Phys. Discuss.*, **13**(7), 19895–19919.
- Andersson, M. E., Verronen, P. T., Wang, S., Rodger, C. J., Clilverd, M. A., and Carson, B. R. (2012). *J. Geophys. Res.*, **117**, D09304.
- Baker, D. N., Kanekal, S. G., Li, X., Monk, S. P., Goldstein, J., and Burch, J. L. (2004). *Nature*, **432**, 878–881.
- Baldwin, M. P., Stephenson, D. B., Thompson, D. W. J., Dunkerton, T. J., Charlton, A. J., and O’Neill, A. (2003). *Science*, **301**, 636–640.
- Baumgaertner, A. J. G., Seppälä, A., Joeckel, P., and Clilverd, M. A. (2011). *Atmos. Chem. Phys.*, **11**(9), 4521–4531.
- Bochníček, J. and Hejda, P. (2005). *J. Atmos. Sol. Terr. Phys.*, **67**(1-2), 17–32.
- Borovsky, J. E. and Denton, M. H. (2006). *J. Geophys. Res.*, **111**, A07S08.
- Brasseur, G. P. and Solomon, S. (2005). *Aeronomy of the Middle Atmosphere* (3rd revised and enlarged edn). Springer, Dordrecht.
- Clilverd, M. A., Rodger, C. J., Danskin, D., Usanova, M. E., Raita, T., Ulich, Th., and Spanswick, E. L. (2012). *J. Geophys. Res.*, **117**, A12213.
- Clilverd, M. A., Seppälä, A., Rodger, C. J., Mlynczak, M. G., and Kozyra, J. U. (2009). *J. Geophys. Res.*, **114**, A04305.
- Crutzen, P. J. (1970). *Q. J. R. Meteorol. Soc.*, **96**, 320–325.
- Daae, M., Espy, P. J., Nesse Tyssøy, H., Newnham, D. A., Stadsnes, J., and Søråas, F. (2012). *Geophys. Res. Lett.*, **39**, L21811.
- Green, J. C., Onsager, T. G., O’Brien, T. P., and Baker, D. N. (2004). *J. Geophys. Res.*, **109**, A12211.
- Hargreaves, J. K. (1992). *The solar-terrestrial environment*. Cambridge Atmospheric and Space Science Series. Cambridge University Press, Cambridge, UK.
- Harvey, V. L., Randall, C. E., and Hitchman, M. H. (2009). *J. Geophys. Res.*, **114**, D22105.
- Hendry, A. T., Rodger, C. J., Clilverd, M. A., Thomson, N. R., Morley, S. K., and Raita, T. (2012). *Geophys. Monogr. Ser.*, **199**, 213–223.
- Horne, R. B. (2002). In *The contribution of wave-particle interactions to electron loss and acceleration in the Earth’s radiation belts during geomagnetic storms* (ed. W. R. Stone), pp. 801–828.
- Horne, R. B., Thorne, R. M., Shprits, Yu. Y., Meredith, N. P., Glauert, S. A., Smith, A. J., Kanekal, S. G., Baker, D. N., Engebretson, M. J., Posch, J. L., Spasojevic, M., Inan, U. S., Pickett, J. S., and Decreau, P. M. E. (2005). *Nature*, **437**, 227–230.
- Jöckel, P., Tost, H., Pozzer, A., Brühl, C., Buchholz, J., Ganzeveld, L., Hoor, P., Kerkweg, A., Lawrence, M. G., Sander, R., Steil, B., Stiller, G., Tanarhte, M., Taraborrelli, D., Van Aardenne, J., and Lelieveld, J. (2006). *Atmos. Chem. Phys.*, **6**,

20 References

- 5067–5104.
- Kennel, C. F. and Petschek, H. E. (1966). *Journal of Geophysical Research: Space Physics (1978–2012)*, **71**(1), 1–28.
- Lam, H. L., Boteler, D. H., Burlton, B., and Evans, J. (2012). *Space Weather*, **10**, S10003.
- Langematz, U., Kunze, M., Krüger, K., Labitzke, K., and Roff, G. L. (2003). *J. Geophys. Res.*, **108**, 4027.
- Li, Y., Lu, H., Jarvis, M. J., Clilverd, M. A., and Bates, B. (2011). *J. Geophys. Res.*, **116**, 16109.
- Lichtenberger, J., Clilverd, M. A., Heilig, B., Vellante, M., Manninen, J., Rodger, C. J., Collier, A. B., Jørgensen, A. M., Reda, J., Holzworth, R. H., Friedel, R., and Simon-Wedlund, M. (2013). *J. Space Weather Space Clim.*, **3**, A23.
- Lu, H., Jarvis, M. J., and Hibbins, R. E. (2008). *J. Geophys. Res.*, **113**(D23).
- Meredith, N. P., Horne, R. B., Thorne, R. M., and Anderson, R. R. (2003). *Geophys. Res. Lett.*, **30**(16), 1871.
- Millan, R. M. and Baker, D. N. (2012). *Space Sci. Rev.*, **173**, 103–131.
- Millan, R. M. and Thorne, R. M. (2007). *J. Atmos. Sol. Terr. Phys.*, **69**(3), 362–377.
- Morley, S. K., Friedel, R. H. W., Cayton, T. E., and Noveroske, E. (2010a). *Geophys. Res. Lett.*, **37**, L06102.
- Morley, S. K., Friedel, R. H. W., Spanswick, E. L., Reeves, G. D., Steinberg, J. T., Koller, J., Cayton, T., and Noveroske, E. (2010b). *Proceedings of the Royal Society A: Mathematical, Physical and Engineering Science*, **466**, 3329–3350.
- Newnham, D. A., Espy, P. J., Clilverd, M. A., Rodger, C. J., Seppälä, A., Maxfield, D. J., Hartogh, P., Holmén, K., and Horne, R. B. (2011). *Geophys. Res. Lett.*, **38**, L20104.
- Newnham, D. A., Espy, P. J., Clilverd, M. A., Rodger, C. J., Seppälä, A., Maxfield, D. J., Hartogh, P., Straub, C., Holmén, K., and Horne, R. B. (2013). *J. Geophys. Res.*, **118**, 7874–7885.
- Omura, Y. and Zhao, Q. (2013). *J. Geophys. Res.*, **118**(8), 5008–5020.
- Randall, C. E. and Harvey, V. L. and Manney, G. L. and Orsolini, Y. J. and Codrescu, M. and Sioris, C. E. and Brohede, S. and Haley, C. S. and Gordley, L. L. and Zawodny, J. M. and Russell III, J. M. (2005). *Geophys. Res. Lett.*, **32**, L05802.
- Randall, C. E., Harvey, V. L., Singleton, C. S., Bailey, S. M., Bernath, P. F., Codrescu, M., Nakajima, H., and Russell III, J. M. (2007). *J. Geophys. Res.*, **112**, D08308.
- Randall, C. E., Harvey, V. L., Siskind, D. E., France, J., Bernath, P. F., Boone, C. D., and Walker, K. A. (2009). *Geophys. Res. Lett.*, **36**, L18811.
- Rees, M. H. (1989). *Physics and chemistry of the upper atmosphere*. Cambridge atmospheric and space science series. Cambridge University Press, Cambridge, UK.
- Reeves, G. D., McAdams, K. L., Friedel, R. H. W., and O'Brien, T. P. (2003). *Geophys. Res. Lett.*, **30**, 1529.
- Renwick, J. and Thompson, D. (2006). *Water Atmos*, **14**(2).
- Rodger, C. J., Clilverd, M. A., Seppälä, A., Thomson, N. R., Gamble, R. J., Parrot, M., Sauvaud, J.-A., and Ulich, Th. (2010). *J. Geophys. Res.*, **115**, A11320.
- Rodger, C. J., Clilverd, M. A., Thomson, N. R., Gamble, R. J., Seppälä, A., Turunen, E., Meredith, N. P., Parrot, M., Sauvaud, J.-A., and Berthelier, J.-J. (2007). *J.*

- Geophys. Res.*, **112**, 11307.
- Rozanov, E., Callis, L. B., Schlesinger, M., Yang, F., Andronova, N., and Zubov, V. (2005). *Geophys. Res. Lett.*, **32**, L14811.
- Scaife, A. A., Knight, J. R., Vallis, G. K., and Folland, C. K. (2005). *Geophys. Res. Lett.*, **32**(18), L18715.
- Seppälä, A., Lu, H., Clilverd, M. A., and Rodger, C. J. (2013). *J. Geophys. Res.*, **118**(5), 2169–2183.
- Seppälä, A., Randall, C. E., Clilverd, M. A., Rozanov, E., and Rodger, C. J. (2009). *J. Geophys. Res.*, **114**, A10312.
- Seppälä, A., Verronen, P. T., Clilverd, M. A., Randall, C. E., Tamminen, J., Sofieva, V. F., Backman, L., and Kyrölä, E. (2007). *Geophys. Res. Lett.*, **34**(12), L12810.
- Seppälä, A., Verronen, P. T., Kyrölä, E., Hassinen, S., Backman, L., Hauchecorne, A., Bertaux, J.-L., and Fussen, D. (2004). *Geophys. Res. Lett.*, **31**(19), L19107.
- Seppälä, A., Verronen, P. T., Sofieva, V. F., Tamminen, J., Kyrölä, E., Rodger, C. J., and Clilverd, M. A. (2006). *Geophys. Res. Lett.*, **33**(7), L07804.
- Simpson, I. R., Blackburn, M., and Haigh, J. D. (2009). *J. Atmos. Sci.*, **66**, 1347.
- Siskind, D. E., Bacmeister, J. T., Summers, M. E., and Russell, J. M. III (1997). *J. Geophys. Res.*, **102**(D3), 3527–3545.
- Solomon, S. C., Barth, C. A., and Bailey, S. M. (1999). *Geophys. Res. Lett.*, **26**(9), 1259–1262.
- Spjeldvik, W. N. and Rothwell, P. L. (1985). In *Handbook of Geophysics and the Space Environment* (ed. A. S. Jursa). Air Force Geophysics Laboratory, Springfield, Virginia.
- Summers, D., Ni, B., and Meredith, N. P. (2007). *J. Geophys. Res.*, **112**(A4), A04207.
- Summers, D. and Thorne, R. M. (2003). *Journal of Geophysical Research: Space Physics (1978–2012)*, **108**(A4), 1143.
- Thorne, R. M. (2010). *Geophys. Res. Lett.*, **37**(2), 22107.
- Turunen, E., Verronen, P. T., Seppälä, A., Rodger, C. J., Clilverd, M. A., Tamminen, J., Enell, C.-F., and Ulich, Th. (2009). *J. Atmos. Sol. Terr. Phys.*, **71**, 1176–1189.
- Van Allen, J. A. and Frank, L. A. (1959). *Nature*, **183**, 430–434.
- Verronen, P. T., Andersson, M. E., Rodger, C. J., Clilverd, M. A., Wang, S., and Turunen, E. (2013). *J. Geophys. Res.*, **118**, 11419–11428.
- Verronen, P. T. and Lehmann, R. (2013). *Ann. Geophys.*, **31**(5), 909–956.
- Verronen, P. T., Rodger, C. J., Clilverd, M. A., and Wang, S. (2011). *J. Geophys. Res.*, **116**, D07307.
- Verronen, P.T., Seppälä, A., Clilverd, M.A., Rodger, C.J., Kyrölä, E., Enell, C.-F., Ulich, Th., and Turunen, E. (2005). *J. Geophys. Res.*, **110**, A09S32.
- Walt, M. (1984). *Introduction to Geomagnetically Trapped Radiation*. Cambridge University Press, Cambridge, UK.